Dose image prediction for range and width verifications from carbon ion-induced secondary electron bremsstrahlung x-rays using deep learning workflow

Mitsutaka Yamaguchi*
Takasaki Advanced Radiation Research Institute, Quantum Beam Science Research Directorate, National Institutes for Quantum and Radiological Science (QST), Takasaki, Japan

Chih-Chieh Liu*
Department of Biomedical Engineering, University of California, Davis, CA, USA

Hsuan-Ming Huang
Institute of Medical Device and Imaging, College of Medicine, National Taiwan University, Taipei City, Taiwan

Takuya Yabe
Radiological and Medical Laboratory Sciences, Nagoya University Graduate School of Medicine, Nagoya, Japan

Takashi Akagi
Hyogo Ion Beam Medical Center, Tatsuno, Japan

Naoki Kawachi
Takasaki Advanced Radiation Research Institute, Quantum Beam Science Research Directorate, National Institutes for Quantum and Radiological Science (QST), Takasaki, Japan

Seiichi Yamamoto[a)]
Radiological and Medical Laboratory Sciences, Nagoya University Graduate School of Medicine, Nagoya, Japan

Purpose: Imaging of the secondary electron bremsstrahlung (SEB) x rays emitted during particle-ion irradiation is a promising method for beam range estimation. However, the SEB x-ray images are not directly correlated to the dose images. In addition, limited spatial resolution of the x-ray camera and low-count situation may impede correctly estimating the beam range and width in SEB x-ray images. To overcome these limitations of the SEB x-ray images measured by the x-ray camera, a deep learning (DL) approach was proposed in this work to predict the dose images for estimating the range and width of the carbon ion beam on the measured SEB x-ray images.

Methods: To prepare enough data for the DL training efficiently, 10,000 simulated SEB x-ray and dose image pairs were generated by our in-house developed model function for different carbon ion beam energies and doses. The proposed DL neural network consists of two U-nets for SEB x ray to dose image conversion and super resolution. After the network being trained with these simulated x-ray and dose image pairs, the dose images were predicted from simulated and measured SEB x-ray testing images for performance evaluation.

Results: For the 500 simulated testing images, the average mean squared error (MSE) was 2.5×10^{-5} and average structural similarity index (SSIM) was 0.997 while the error of both beam range and width was within 1 mm FWHM. For the three measured SEB x-ray images, the MSE was no worse than 5.5×10^{-3} and SSIM was no worse than 0.980 while the error of the beam range and width was 2 mm and 5 mm FWHM, respectively.

Conclusions: We have demonstrated the advantages of predicting dose images from not only simulated data but also measured data using our deep learning approach. © *2020 American Association of Physicists in Medicine* [https://doi.org/10.1002/mp.14205]

1. INTRODUCTION

In particle therapy, a small beam range difference could be critical because normal tissues might be irradiated with unnecessary radiation dose if the ranges are not precisely measured. Techniques are being developed to measure the ranges from outside of the subject during beam irradiation.[1–22] In these techniques, imaging of the secondary electron bremsstrahlung (SEB) x ray emitted during proton or carbon ion irradiation is also a promising method for range estimation[23] and we have so far developed low-energy x-ray cameras and conducted the imaging of SEB x ray of proton[24,25] or carbon ion[26] by using these low-energy x-ray cameras. With the improvement of the camera's performance, it

could be used for imaging with almost clinical dose level of carbon ion and real-time imaging of the carbon ion beam was realized.[27] However, the distributions of the SEB x-ray images are different from the dose images.[23–27] In addition, limited spatial resolution of the x-ray camera and low-count situation may impede the correctness of the beam range and width estimation in the x-ray images. The curve-fitting approach was used in our previous study for the end of the range part of the depth profiles measured from the SEB x-ray images, but high deviations were observed dependent on the selected areas.[27] Furthermore, the estimated widths of the measured x-ray images were greater than the carbon ion beam widths.[27] The SEB x-ray imaging would be more useful for carbon ion therapy when the accuracy of range and width estimation is improved in the SEB x-ray images.

Deep learning (DL) has been successfully applied to different modality image conversion in the medical imaging field. DL was recently used to enhance the quality of the estimated attenuation map from the maximum likelihood activity and attenuation reconstruction (MLAA).[28,29] In proton therapy dosimetry, DL was also recently proposed to predict dose images from the simulated PET data from proton-induced positron emitters.[30] A similar study was conducted using maximum likelihood expectation maximization (MLEM) algorithm to estimate dose images from the simulated PET data from proton-induced positron emitters.[31] Although both of these approaches could successfully derive the dose distribution from simulated PET images, the characteristics of prompt x-ray images are very different and might be more challenging for dose image conversion. Since the SEB x-ray images are not linearly correlated to carbon ion dose images, we proposed to convert SEB x-ray images to dose image for the range and width verification using a DL approach.

The U-net[32] was chosen for its advantage of extracting the informative multiscale features from the network inputs to resemble the training targets during the training phase. To improve the accuracy of the range and width estimation, our proposed neural network model consists of two U-nets, first one for SEB x-ray to dose image conversion and second for improving the spatial resolution of the dose images (super resolution), which is limited by the intrinsic spatial resolution of the x-ray camera. The matrix size of the final predicted dose image is 25 times more than that of the network inputs.

It is important to note that DL-based approaches require a large amount of training data to ensure the generalization. However, measuring a sufficient amount of data is unfortunately not feasible in proton or carbon ion therapy because of the limited beam time for SEB x-ray imaging experiments using the clinical particle therapy systems. Although the conventional Monte Carlo simulations used in our previous study[27] could already be able to generate small amount of data, it is tremendously computation intensive and time consuming. Therefore, we have developed a dedicated model function with some parameters extracted from the measured data by the x-ray camera to accelerate the whole data generation process. The proposed neural network was trained with these realistic simulated data and successfully deployed to both simulated and measured testing data of noisy SEB x-ray images. The ranges and widths of carbon ion beams could be estimated from the DL-predicted dose images.

2. MATERIALS AND METHODS

2.A. SEB x-ray images during carbon ion irradiations used for the estimations

In the present study, we used the experimental data already reported in Ref. [27]. Schematic drawing of SEB x-ray images by an x-ray camera during carbon ion irradiation is shown in Fig. 1. To measure SEB x-ray images, an x-ray camera was built with a $20 \times 20 \times 0.5$ mm thick YAP (Ce) plate optically coupled to a 25 mm square high quantum efficiency (HQE) cross wire anode type position sensitive photomultiplier tube (PSPMT) (R8900-100-C12, Hamamatsu Photonics, Japan) and contained in 2 cm thick tungsten shield. A 1.5-mm diameter pinhole was used for the imaging because of the high sensitivity. The distance from the x-ray camera to the phantom was 50 cm.[27] The system spatial resolution and sensitivity of the developed x-ray camera at 50 cm from the subject for 35 keV x rays were 23 mm FWHM and 6.9×10^{-7}, respectively. For each imaging of x rays, the acquisition time of the x-ray camera was set to 3 min. During the x-ray camera acquisition, the phantom was irradiated by the carbon ion beam. The number of carbon ions was set to 7.5×10^9 for three different energies, that is, 241.5 MeV/n, 216 MeV/n, and 190 MeV/n. The number of carbon ion particles was ~ 2.3 times of the average clinical dose level.[33]
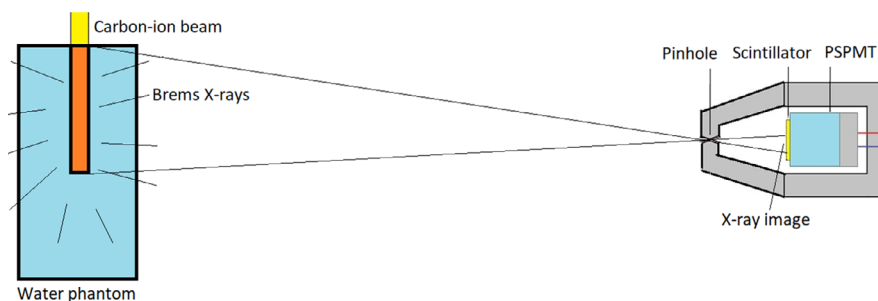

FIG. 1. Schematic drawing of SEB x-ray images by x-ray camera during carbon ion irradiation. [Color figure can be viewed at wileyonlinelibrary.com]
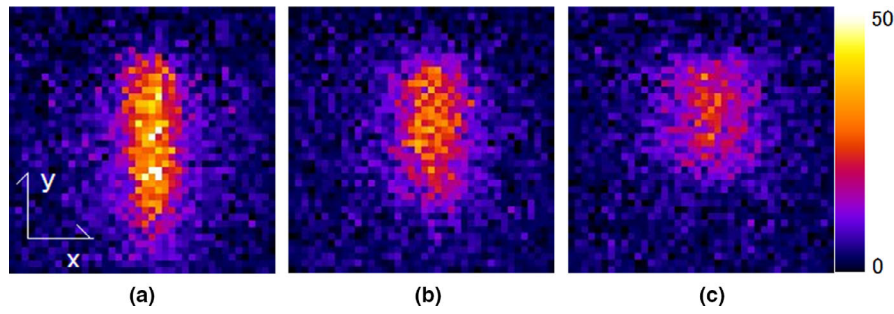
FIG. 2. Measured SEB x-ray images during carbon ion irradiation: 241.5 MeV/n (a), 216 MeV/n (b), and 190 MeV/n (c). [Color figure can be viewed at wileyon linelibrary.com]

TABLE I. List of carbon ions used for imaging experiment for SEB x-ray.

Energy of carbon ion	Lateral width of the beam	Range of the beam
241.5 MeV/n	19 mm FWHM	119 mm
216 MeV/n	28 mm FWHM	99 mm
190 MeV/n	38 mm FWHM	79 mm

The three noisy measured SEB x-ray images for the evaluation of the DL are shown in Fig. 2. Numbers of the counts in the images were 8–11 k counts. The ranges and widths of the carbon ion beams for these three different energies in water were estimated by the planning system of the carbon ion therapy system listed in Table I.

2.B. SEB x-ray images and dose images generated by simulation used for DL

2.B.1. Monte Carlo simulation toolkit

Monte Carlo (MC) simulations were performed using the Particle and Heavy Ion Transport code System (PHITS)[34] version 3.10. The input parameters for the calculation of gamma decays emitted from residual nuclei were set to use the ENSDF-based isometric transition and isomer production model to calculate prompt gamma photons precisely. A transport algorithm for electrons, positrons, and photons based on the EGS5 was used in the simulations. Cut-off energies of electrons, positrons, photons, and neutrons were set to 10 keV, 10 keV, 10 keV, and 1.0×10^{-7} keV, respectively.

2.B.2. SEB x-ray images

DL-based approaches generally require preparing a large amount of training data. As a method to prepare training data of SEB x-ray images, it is conceivable to use MC simulation as performed in Ref. [27]. However, the simulation is computationally intensive, and it is difficult to prepare a large amount of training data only using the MC simulation. Therefore, we designed a model function that replicates the measured data by the x-ray camera and is utilized to generate training data more efficiently.

As described in Ref. [24], the images of the low-energy x-ray emitted from proton-beam trajectories were well

explained by the sum of the SEB and background low signal components (BG). Also in the case of the carbon ion beams, we assumed that it is represented by the sum of the two components as follows:

$$f(x, y) = f_{\text{SEB}} + f_{\text{BG}}, \tag{1}$$

where $f(x, y)$ represents the number of the energy depositions per carbon ion injection for the pixel located at the coordinate of (x, y). The terms f_{SEB} and f_{BG} in the right side represent the SEB and BG components, respectively.

We estimated the distribution of the BG component by MC method using PHITS. Figure 3(a) shows the simulation geometry, which consists of a water phantom and an x-ray camera. This geometry was decided to reproduce the experimental setup described in Section 2.1, which is the same as that in Ref. [27]. The distribution of the BG component was made by recording the number of events other than SEB detection events having energy depositions from 30 to 60 keV in all pixels in the scintillation crystal in the simulation. The BG component is generated by partial energy detection of higher energy gamma rays generated by the beams. Figure 3(b) and (c) show the projections of the BG component on x- and y-axis. The number of the injected carbon ions in the simulation was 7.5×10^9. The injection energy was 241.5 MeV/n. In order to avoid recording the SEB detection events, secondary electron generation was suppressed in the simulation. As shown in Fig 3(a) and (b), the BG component f_{BG} was estimated to have flat distributions.

The SEB component was expressed in this work as:

$$f_{\text{SEB}}(\xi, \eta) = f_x(\xi) \times f_y(\eta), \tag{2}$$

$$f_x(\xi) = \alpha_x V(\xi; \sigma_x, \gamma_x), \tag{3}$$

$$\xi = x - x_0, \tag{3}$$

$$f_y(\eta) = \alpha_y \int_{-\infty}^{\infty} D(\eta - \eta'; s) V(\eta'; \sigma_y, \gamma_y) d\eta', \tag{4}$$

$$\eta = y_0 - y, \tag{5}$$

where x_0 and y_0 correspond to the x-coordinate of the beam axis and the y-coordinate of the injection surface of the water phantom, respectively. The profile $V(x; \sigma, \gamma)$ represents the Voigt profile, which is calculated by the convolution of
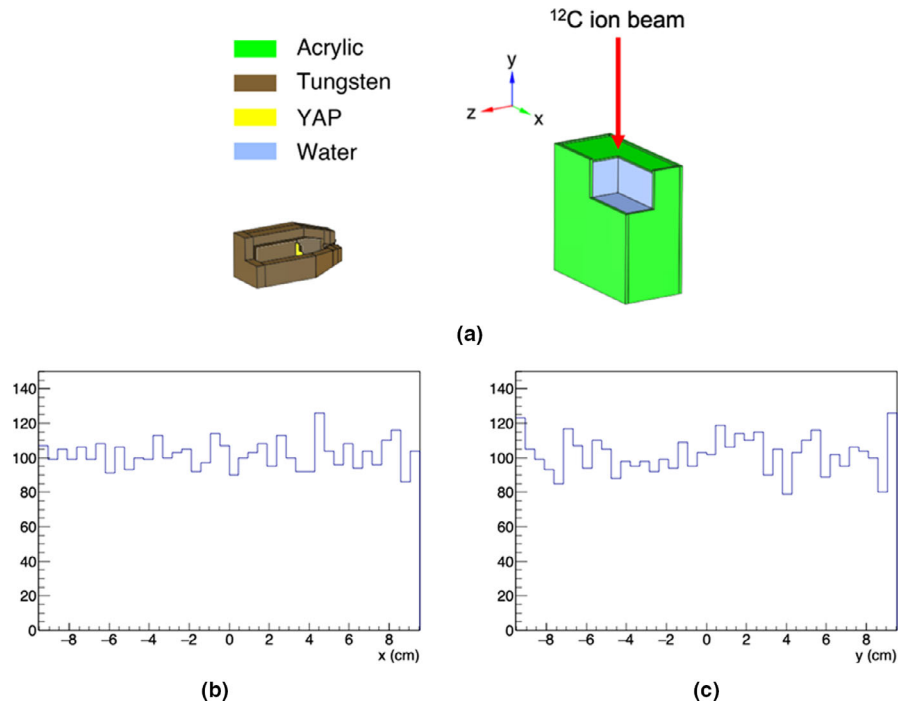
FIG. 3. (a) The simulation geometry for the BG component calculation and the projections of the BG component on (b) *x*- and (c) *y*-axis. [Color figure can be viewed at wileyonlinelibrary.com]

Gaussian $G(x; \sigma)$ and Lorentzian $L(x; \gamma)$ profiles as follows:

$$V(x; \sigma, \gamma) = \int_{-\infty}^{\infty} G(x'; \sigma) L(x - x'; \gamma) dx', \qquad (7)$$

$$G(x; \sigma) = \frac{e^{-x^2/(2\sigma^2)}}{\sigma\sqrt{2\pi}}, \qquad (8)$$

$$L(x; \gamma) = \frac{\gamma}{\pi(x^2 + \gamma^2)}. \qquad (9)$$

The Gaussian and Lorentzian profiles in the Voigt profiles express the beam profiles and scattering and absorption effects of SEB in the water phantom, respectively.

The profile $D(\eta; s)$ represents the depth profile of the number of SEB generation in water along *y* at any *x* and *z*, where η means the depth from the injection surface of the water and *s*, which fulfills $s \geq 0$, means the length of the range shift occurring by changes of the beam energy. For example, *s* takes 0, 2, and 4 cm when the beam energy is 241.5, 216, and 190 MeV/n, respectively. The energy of the carbon ion beam *E* and the range shift *s* fulfill following equation:

$$E = \frac{2897.0 - 143.3 \times s - 3.181 \times s^2}{12}, \qquad (10)$$

where the units of *E* and *s* are MeV/n and cm, respectively. We deduced Eq. (10) by means of PHITS simulations.

The depth profile for $s = 0$, that is, $D(\eta; 0)$ has been calculated by an MC simulation using PHTIS, where carbon ions having the energy of 241.5 MeV/n were injected into the water phantom and generation depths of SEB having the

energies from 30 to 60 keV were recorded. Figure 4 represents the simulation result of the depth profile $D(\eta; 0)$. To reduce computational burden, instead of doing simulations with various *s* other than 0, we approximated the profile $D(\eta; s)$ as:

$$D(\eta; s) \approx \begin{cases} 0, & \eta < 0 \\ D(\eta + s; 0), & \eta \geq 0 \end{cases}. \qquad (11)$$

From the experimental data in Section 2.1, the BG component for the experimental data, which we represent $f_{BG}^{(exp)}$, was estimated using some peripheral pixel's counts as:

$$f_{BG}^{(exp)} = \sum_{j=j_{min}}^{j_{max}} \left(N_{i_{min},j} + N_{i_{min}+1,j} + N_{i_{max}-1,j} + N_{i_{max},j} \right), \qquad (12)$$
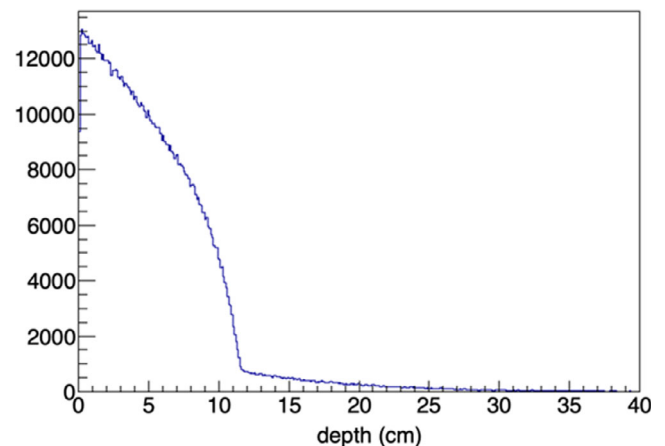

FIG. 4. The simulation result of the depth profile $D(\eta; 0)$. [Color figure can be viewed at wileyonlinelibrary.com]

where N_{ij} represents the count of the pixel in the i-th column and the j-th low. We did not include the pixels where might be attributed to SEB component instead of background low signal component. By fitting the deduced values with a linear function, the BG component could be represented by the following equation:

$$f_{BG} = 6379 - 7.679 \times E. \tag{13}$$

The estimated BG component $f_{BG}^{(exp)}$ was subtracted from the experimental data in Section 2.1 to estimate the SEB component in experimental data, which is represented as $f_{SEB}^{(exp)}$. Next, by fitting the x-axis projection of $f_{SEB}^{(exp)}$ with Eq. (3), the parameters x_0, α_x, and γ_x were deduced where the parameter σ_x was fixed to the following value:

$$\sigma_x = 4.639 - 0.016 \times E, \tag{14}$$

which represents the energy-dependent beam diameter. By fitting the deduced γ_x, it was represented by a linear function:

$$\gamma_x = 6.592 - 0.01678 \times E. \tag{15}$$

Thirdly, by fitting the y-axis projection of $f_{SEB}^{(exp)}$ with Eq. (5), the parameters y_0, α_y, σ_y, and γ_y were deduced. By fitting the deduced values of the parameters, energy dependences of the parameters y_0, σ_y, and γ_y are represented as linear functions of the injection energy E as:

$$y_0 = 7.227 - 0.01249 \times E, \tag{16}$$

$$\sigma_y = -2.752 + 0.01984 \times E, \tag{17}$$

$$\gamma_y = 5.575 - 0.01908 \times E. \tag{18}$$

We could simulate the SEB x-ray images for any injection energy, any beam width, and any beam position by randomly filling two-dimensional histograms using the model function $f(x, y)$ as probability density function. Although the model function was designed based on the same experimental data that were used in the evaluation for DL, the function would not produce exactly the same images as the data due to the random variables and different energy settings. In Fig. 5, projections of the experimental data and the model curves simulated using the model function on x- and y-axis are shown. For all three energies, the model curves could well replicate the experimental data.

For the study of deep learning in Section 2.3, we simulated 10,000 SEB x-ray images using the model function with randomly changing the parameters of the model function according to uniform probability distribution. The changed parameters and the ranges of the change were summarized in Table II. The injection energy of the carbon ion beam was decided using Eq. (10). The maximum and minimum of the injection energies were 241.5 and 175.1 MeV/n, which correspond to the 0.0- and 5.0-cm range shifts for the carbon ion beam having the energy of 241.5 MeV/n, respectively. The parameters f_{BG}, σ_x, γ_x, y_0, σ_y, and γ_y were changed with the injection energy E according to the linear functions deduced above. Total count in each SEB image S_{SEB} was decided by the following linear function of injection energy E as:
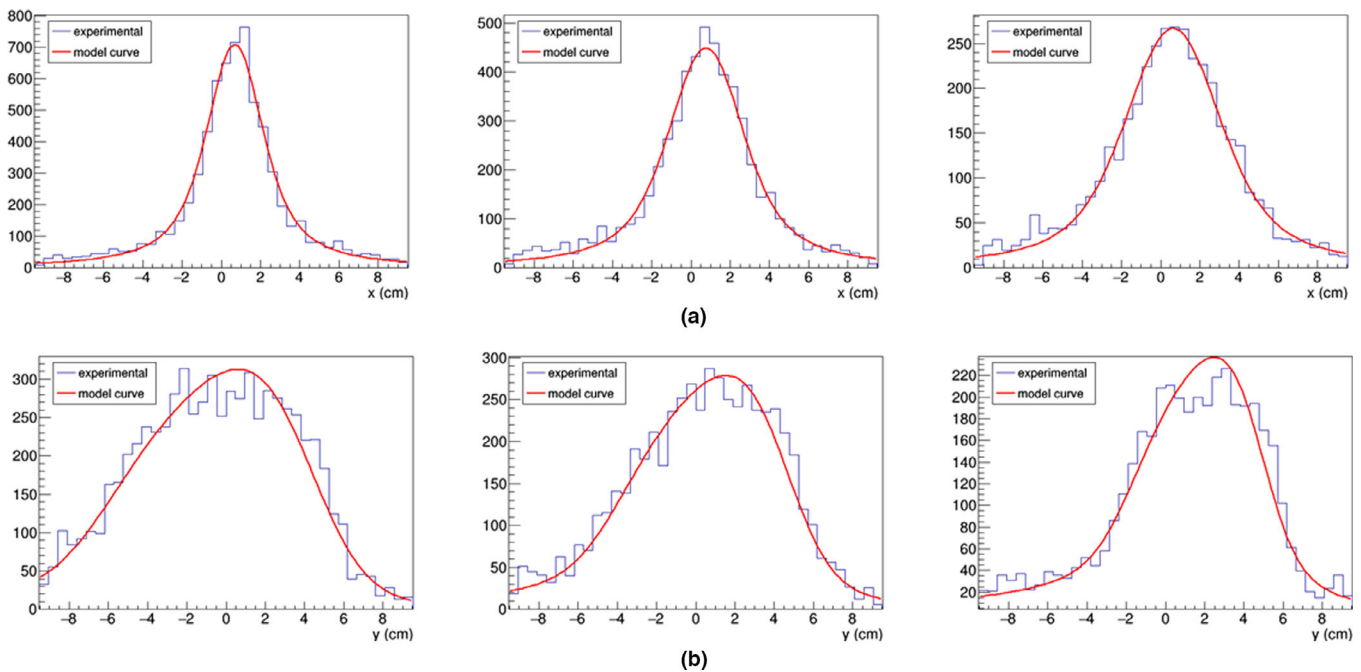

FIG. 5. Projections of the experimental data (blue lines) and the model curves simulated using the model function (red curves) on (a) x- and (b) y-axis. The left, central, and right panels represent for the incident energies of 241.5, 216, and 190 MeV/n, respectively. [Color figure can be viewed at wileyonlinelibrary.com]

TABLE II. Changed parameters and ranges of the change.

Parameter	Range of the change
s	0–5 cm
x_0	−2 to 2 cm

$$S_{\text{SEB}} = -6632 + 56.29 \times E, \tag{19}$$

which were deduced by fitting the three experimental total SEB counts $S_{\text{SEB}}^{(\text{exp})}$ defined as:

$$S_{\text{SEB}}^{(\text{exp})} = \sum f_{\text{SEB}}^{(\text{exp})}, \tag{20}$$

with a linear function, where the sum in the right side of Eq. (20) is taken over the all pixels.

2.B.3. Dose images

Because the computational burden for the calculation of dose images is much smaller than that for the SEB x-ray images, the dose images were prepared directly by performing MC simulations. Simulation geometry of the water phantom was made to be geometrically the same as that used in the experiment and a carbon ion beam was injected into the water phantom from the upper side. The intensity distributions of the beams in the direction perpendicular to the beam axis were Gaussian distribution having the width parameter of σ_x represented as Eq. (14). The dose images were made by recording the projections of energy depositions in the water phantom on *xy*-plane. The sizes of the dose images were the same as the field of view (FOV) of the x-ray camera. Two matrix sizes of dose images, 40×40 and 200×200, were made for each simulation.

2.C. DL-based approach for SEB x ray to dose image conversion and super resolution

The simulated SEB x-ray images and dose images were first set to 40×40 and the pixel size of 4.76 mm to match

the same dimension of the SEB x-ray images from the camera in the measurements. These simulated SEB x-ray images and carbon ion distributions were prepared as training inputs and targets, respectively. Furthermore, we would like to take the advantage of the simulations to improve the resolution of the dose predictions by using finer spatial resolution simulated dose images (200×200) as training targets. The setup of the proposed neural network architecture, data preparation, training strategy, and computation platform are described in this section.

2.C.1. Neural network architecture

Our proposed DL network consists of two standard U-nets with four levels shown in Fig. 6. Both of the U-nets in our network are identical. The root features are 16 on the top level and doubled every level down. There are two 3×3 convolutional layers followed by a Rectified Linear Unit (ReLU) activation function every level each in the encoding and decoding processes. The feature maps containing high frequency information are concatenated via the skip connections to the convolutional layers in the decoding process on every level. In the end of each U-net, a 1×1 convolutional layer without activation function reduces the number of the feature maps from the previous layer into one as the network output. The total number of trainable parameters in each U-net is about 5 million. These two U-nets are connected by an upsampling layer to match the dimension of the outputs from the first U-net to that of the targets in the second U-net, that is, 200×200. The purpose of the first U-net is to convert 40×40 SEB x-ray images to 40×40 predicted dose images, whereas that of the second U-net is to enhance the spatial details in the final network outputs as super resolution.

2.C.2. Data preparation and network training

Although the structural features in the SEB x-ray images and dose images are less complex compared to other medical
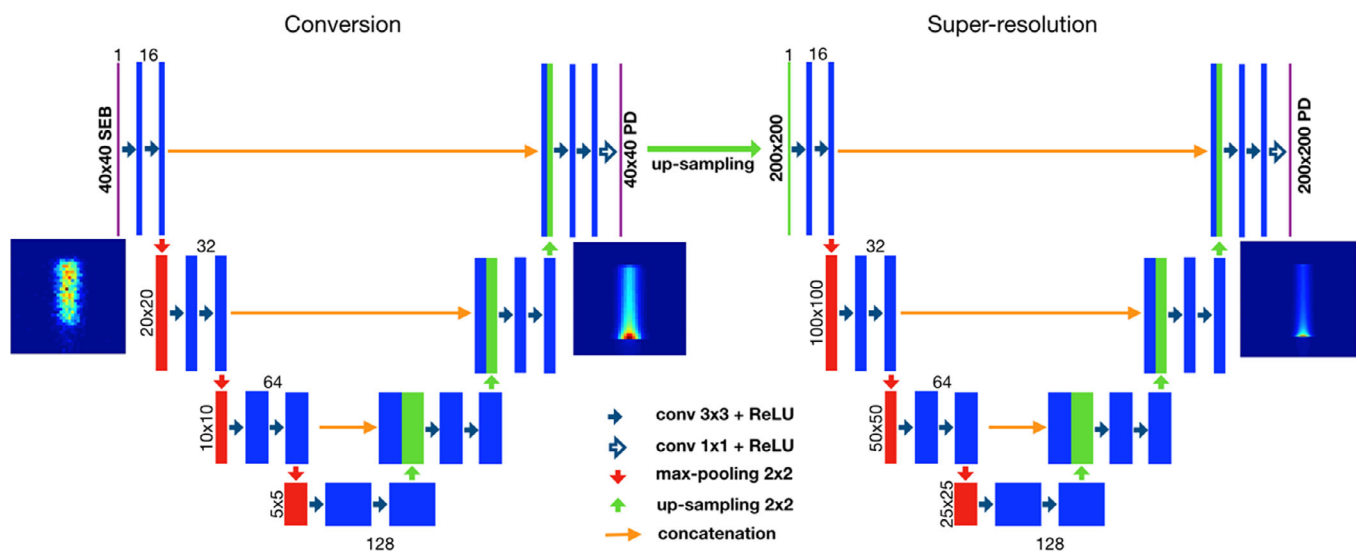

FIG. 6. Double-U-net architecture for SEB x-ray dose image conversion and super resolution. [Color figure can be viewed at wileyonlinelibrary.com]

images, the characteristics of the carbon ion beams have a tremendous impact on the signal-to-noise ratio (SNR) and morphological variation in the dose images. Therefore, a great number of 10,000 SEB x-ray-dose image pairs were generated under the various aforementioned simulation conditions to present essential features to our proposed network during training phase. Moreover, the detector-specific noise was modeled more sophistically for the x-ray camera in the simulations by our in-house developed model function to mitigate the discrepancy when deploying the trained model to the measured SEB x-ray images. There were 9,000 simulated SEB x-ray-dose image pairs grouped as training data, 500 pairs as validation data, and 500 pairs as testing data. Besides evaluating the trained network with the 500 unseen simulated data, three SEB x-ray images measured at the Hyogo Ion Beam Medical Center (Japan) with their corresponding simulated dose images were used to test the network transferability between simulations and real measurements.

The two U-nets in our proposed network theoretically could be trained at once using 40×40 SEB x-ray images as inputs and 200×200 dose images as targets. However, we trained the sole first U-net to obtain 40×40 predicted dose images to study the correlation ability of the network to the two different data dimensions. The trainable parameters in the first U-net in the proposed network were then initialized by the trained network and the whole network was trained with the same training data when the targets were 200×200 dose images. It would accelerate the convergence of training the whole network and consequently obtain better quality of 200×200 predicted dose images.

The loss function was L2-norm for both U-nets and optimized by the Adam optimization algorithm. The default hyperparameters were used, that is, learning rate was $10-6$, beta1 was 0.9, and beta2 was 0.999. The proposed network was implemented using TensorFlow and trained on a NVIDIA Titan XP GPU.

2.C.3. Neural network performance evaluation

To evaluate how the network was trained, it was deployed on the 500 simulated testing SEB x-ray-dose pairs. Three representative data were selected to show the SEB x-ray images, dose images, predicted dose images, and their difference images. The average mean squared error (MSE) and structural similarity index (SSIM) were calculated for measuring the prediction accuracy on full images. In contrast to MSE, SSIM provides a metric that evaluates the similarity on the full image instead of the difference in the image pixels independently. The SSIM of 1 means totally the same between two images, whereas 0 means totally different. SSIM considers luminance, contrast, and structure of the full image, and the further information of SSIM can be found in Ref. [35].

SEB x-ray images were interpolated from 40×40 to 200×200 using public domain software (ImageJ) before the line profiles were drawn for the simulated SEB x-ray images, dose images, and DL-predicted dose images. A vertical line

profile was drawn on the beam to measure the depth profiles and the carbon ion ranges for these three sets of the images. The widths of the line profiles were 10 pixels (~9 mm). The Bragg peak position error is defined as the difference of the Bragg peak position in the predictions and ground truths, while the mean Bragg peak position error was calculated among the 500 simulated testing data. The ranges of the carbon ion beams were estimated from the profiles by calculating the beam lengths at 20% of the peak counts for the representative data. Additionally, the full width at half maximum (FWHM) of the lateral line profiles on the beams was calculated at 38 mm depth of water.

Besides evaluating the trained network on the simulated testing data, the dose images were also predicted from the three measured SEB x-ray images for carbon ion of 241.5 MeV/n, 216 MeV/n, and 190 MeV/n using a 20 cm x 20 cm x 10 cm water phantoms.[27] It would demonstrate the transferability and feasibility of the network trained with the simulated data on real measured data. The same procedure was applied to the measured data as the simulated testing data. The peak positions were also evaluated for the predicted images by DL in both simulated and measured data. Moreover, to check the trained network, the dose images were also predicted from the six measured SEB x-ray images for carbon ion of 241.5 MeV/n irradiated for 10 s (1.25×10^{10} particles) to 17 cm diameter cylindrical phantom.

3. RESULTS

3.A. Neural network performance evaluation

3.A.1. Evaluation of the predicted dose images by DL for simulated SEB x-ray images

The average MSEs of the 500 simulated testing data, SSIMs, and the ratios of these two are listed in Table III. The mean Bragg peak (BP) position errors are also listed in Table III. The MSE was 95 times smaller for 200×200 matrix images.

Three simulated testing data were selected to be representative of the network performance. The simulated SEB x-ray images from three different energies and beam positions are illustrated in [Fig. 7(a)-7(c)], the corresponding dose images in (d)–(f), the predicted dose images in (g)–(i), and the difference images between dose and predicted dose images in (j)–

TABLE III. Average MSE, SSIM, and Bragg peak (BP) position errors for predicted dose images by DL from 500 simulated testing SEB x-ray images.

Matrix size	40×40	200×200	Ratio of 40×40/ 200×200
MSE	2.4×10^{-3}	2.5×10^{-5}	95
SSIM	0.982	0.997	0.98
Mean BP position errors (mm)	2.9×10^{-2}	1.9×10^{-2}	–

MSE, mean squared error; SSIM, structural similarity index.

(l). From [Fig. 7(j)-7(l)], it was confirmed that there was very small difference between dose and predicted dose images from simulated SEB x-ray images.

The depth profiles of the simulated SEB x-ray images, dose images, and DL-predicted dose images are plotted for the individual three representative data in [Figs. 8(a), 8(b) and 8(c)], whereas their lateral profiles are in [Figs. 8(d), 8(e) and 8(f)]. The depth profiles of the SEB simulation data were different from those of the dose or DL-predicted images. This is because there are Bragg peaks at the edges of the carbon ion tracks in the dose distributions, whereas the SEB x-ray distributions have no peaks at the edges because they have larger production cross sections at higher carbon ion energies. Furthermore, while the statistical noise in the dose distributions is negligible, the SEB x-ray distributions have

significant statistical noise due to count limitations. In addition, the x-ray distributions of SEB include the effects of scattering and absorption by water, while not the dose distributions.

The estimated beam ranges for the simulated SEB x-ray images, dose images, DL-predicted dose images, and differences between dose and predicted dose images are summarized in Table IV. The range difference between dose images and generated images by DL was equal to 0 mm.

The beam widths were also estimated for simulated SEB x-ray images, dose images, DL-predicted distributions, and differences between those of the dose and DL-predicted distributions for the three representative data in Table V. The range difference between dose and DL-predicted distributions was equal to 0 mm.
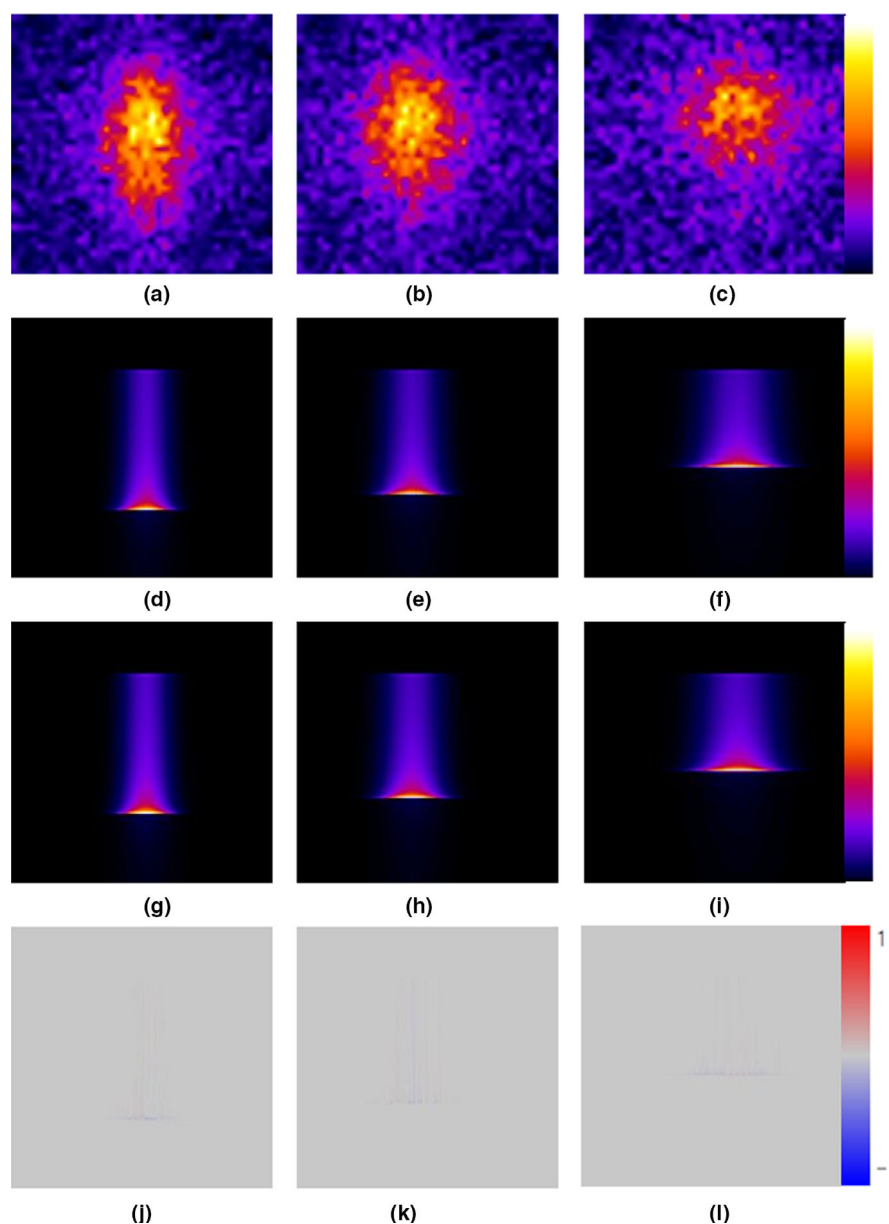

FIG. 7. Simulated SEB x-ray images of No. 1(a), No. 2 (b), No. 3 (c), corresponding dose images for No. 1 (d), No. 2 (e), No. 3 (f), predicted dose images by DL for No. 1 (g), No. 2 (h), No. 3 (i), and difference images between dose and predicted dose images by DL for No. 1 (j), No.2 (k), No. 3 (l). [Color figure can be viewed at wileyonlinelibrary.com]
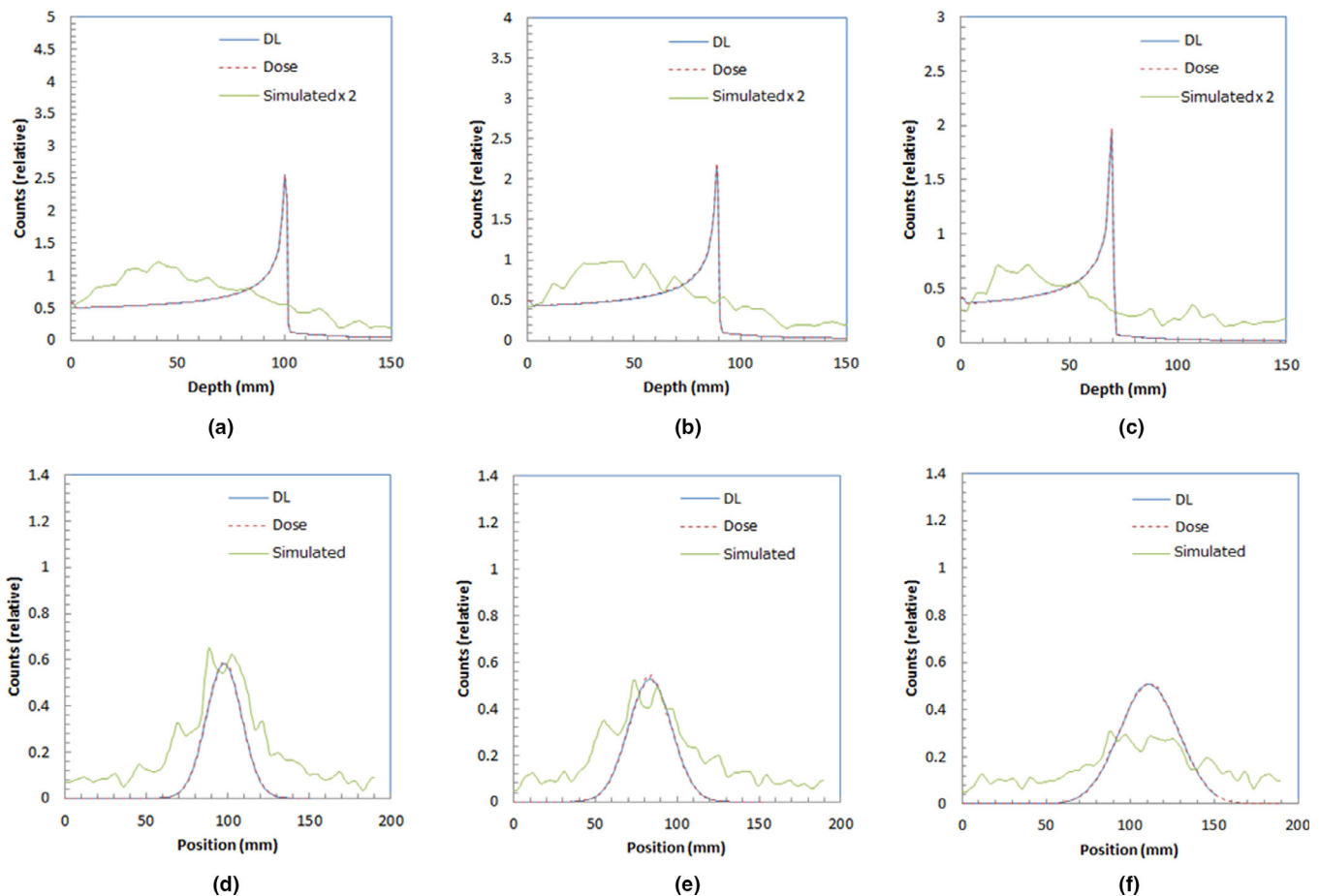
FIG. 8. Depth profiles estimated for simulated SEB x-ray images, dose images, predicted dose images by DL for No. 1 (a), No. 2 (b), and No. 3 (c), and lateral profiles estimated simulated SEB x-ray images, dose images, predicted dose images by DL for No.1 (d), No. 2(e), and No. 3 (f). Simulated x 2 in (a) to (c) means that these profiles are displayed two times larger in vertical value. Vertical axis of each graph is relative counts normalized average value to ~1. [Color figure can be viewed at wileyonlinelibrary.com]

3.A.2. Evaluation of the predicted dose images by DL for measured SEB x-ray images

The measured SEB x-ray images for 241.5 MeV/n, 216 MeV/n, and 190 MeV/n carbon ions from Fig. 2 were upscaled to 200 × 200 and, respectively, shown in [Figs. 9(a)-9(c)], their dose images in [Figs. 9(d)-9(f)], DL-predicted dose images in Figs. 9(g)-9(i), and difference images in [Fig. 9(j)-9(l)]. The measured SEB x-ray images are quite different from those in the simulations in terms of the beam range and the pattern in the background low signal component.

TABLE IV. Estimated beam ranges for simulated SEB x-ray images, dose images, predicted dose images by DL, and difference between dose and DL images with three different energies.

	No. 1	No. 2	No. 3
Simulated SEB x-ray image	138 mm	119 mm	92 mm
Dose image	102 mm	90 mm	70 mm
Predicted dose images by DL	102 mm	90 mm	70 mm
Difference	0 mm	0 mm	0 mm

TABLE V. Estimated beam widths in FWHM for simulated SEB x-ray images, dose images, generated images by DL, and difference between dose and DL images with three different energies.

	No. 1	No. 2	No. 3
Simulated SEB x-ray image	40 mm FWHM	56 mm FWHM	63 mm FWHM
Dose image	26 mm FWHM	31 mm FWHM	41 mm FWHM
Predicted dose images by DL	26 mm FWHM	31 mm FWHM	41 mm FWHM
Difference	0 mm FWHM	0 mm FWHM	0 mm FWHM

The depth profiles of the measured SEB x-ray images, dose images, and DL-predicted dose images are plotted for 241.5 MeV/n, 216 MeV/n, and 190 MeV/n carbon ions in [Figs. 10(a), 10(b) and 10(c)], respectively, whereas the lateral profiles are in [Figs. 10(d), 10(e) and 10(f)].

The estimated beam ranges are summarized for the dose and DL-predicted dose images, measured SEB x-ray images, and differences between those of the dose and DL-predicted dose images for 241.5 MeV/n, 216 MeV/n, and 190 MeV/n
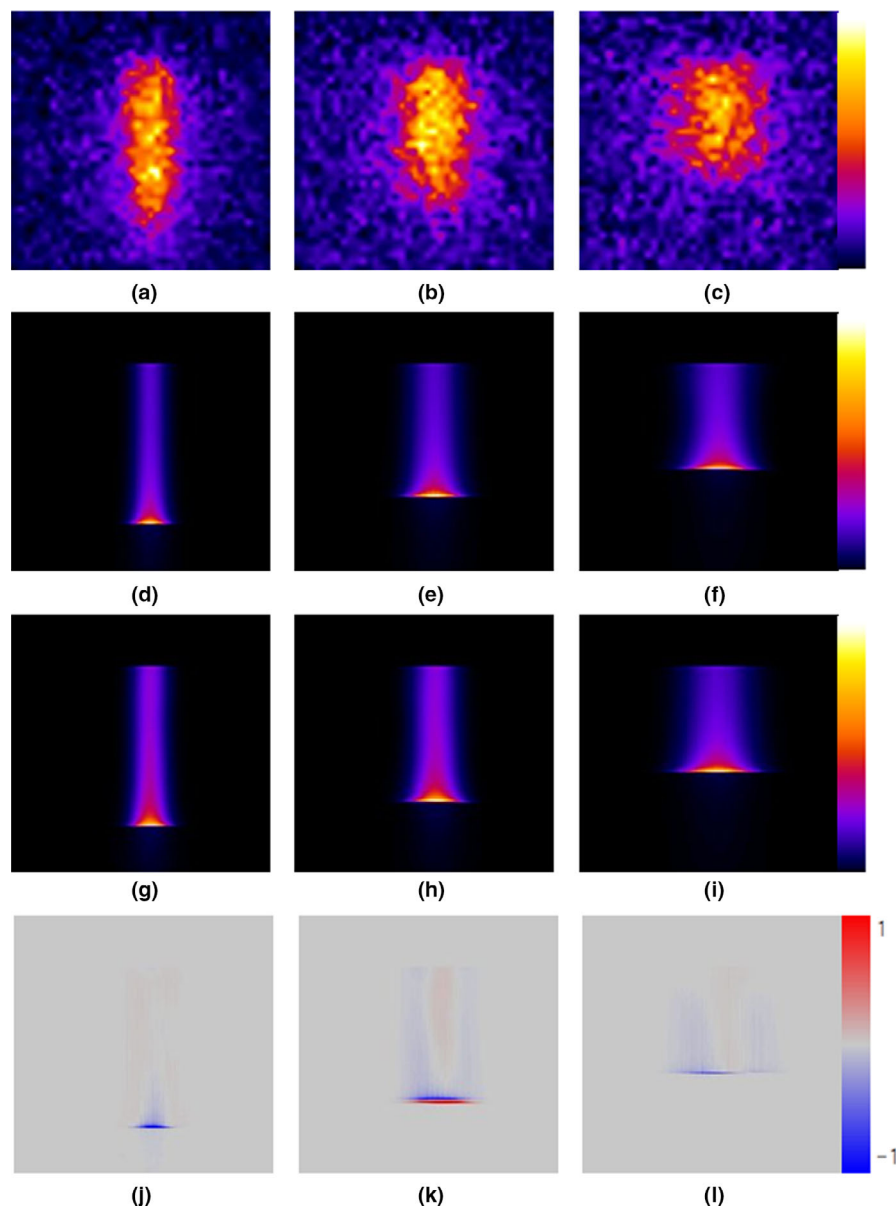
FIG. 9. Measured SEB x-ray images for 241.5 MeV/n (a), 216 MeV/n (b), and 190 MeV/n carbon ions (c), dose images for 241.5 MeV/n (d), 216 MeV/n (e), and 190 MeV/n (f) carbon ions, predicted dose images by DL for 241.5 MeV/n (g), 216 MeV/n (h), and 190 MeV/n (i) carbon ions, and difference images between dose and predicted dose images by DL for 241.5 MeV/n (j), 216 MeV/n (k), and 190 MeV/n (l) carbon ions. [Color figure can be viewed at wileyonline library.com]

carbon ions in Table VI. The range difference between dose and predicted dose images by DL was less than 2 mm.

The estimated beam widths are also summarized for the estimated beam ranges for the dose and DL-predicted dose images, measured SEB x-ray images, and differences between those of the dose and DL-predicted dose images for 241.5 MeV/n, 216 MeV/n, and 190 MeV/n carbon ions in Table VII. The difference of the range between dose and DL-predicted dose images was less than 5 mm.

The MSE and SSIM and Bragg peak (BP) position errors for the predicted dose images by DL from the three measured SEB x-ray images are summarized in Table VIII.

Dose images predicted from the six measured SEB x-ray images for carbon ion of 241.5 MeV/n irradiated for 10 s to 17 cm diameter cylindrical phantom are shown in Supplemental Material. The predicted dose images from the measured SEB x-ray images with different shape of the phantom also showed similar distribution to dose.

4. DISCUSSION

Generating enough amount of measured SEB x-ray images induced by carbon ion beams for deep learning trainings is not only expensive but also time consuming and infeasible. Although conventional MC simulations could in theory generate sufficient training data, it would need 2 hours to generate only one SEB x-ray image on a supercomputer. Therefore, we have developed a dedicated model function
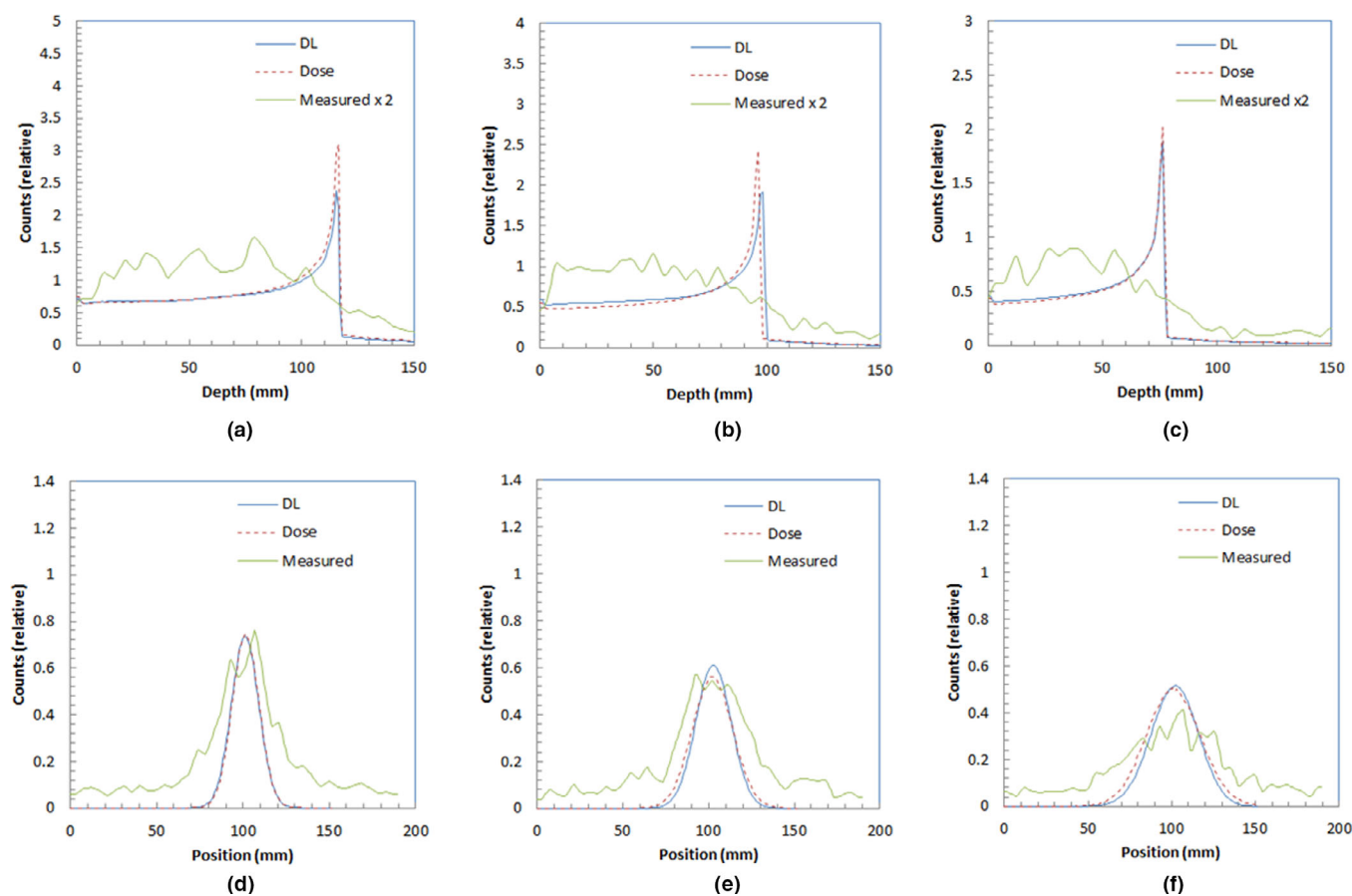
FIG. 10. Depth profiles estimated for image of dose, predicted dose image by DL, and measured image for 241.5 MeV/n (a), 216 MeV/n (b), and 190 MeV/n (c) carbon ions, and lateral profiles estimated for image of dose, predicted dose image by DL, and measured image for 241.5 MeV/n (d), 216 MeV/n (e), and 190 MeV/n (f) carbon ions. [Color figure can be viewed at wileyonlinelibrary.com]

TABLE VI. Estimated beam ranges for three measured SEB x-ray images, dose images, predicted dose images by DL, and difference between dose and DL images.

	241.5 MeV/n	216 MeV/n	190 MeV/n
Measured SEB x-ray image	144 mm	128 mm	92 mm
Dose image	118 mm	98 mm	78 mm
Predicted dose images by DL	118 mm	100 mm	78 mm
Difference	0 mm	2 mm	0 mm

TABLE VII. Estimated beam widths in FWHM for three measured SEB x-ray images, dose images, predicted dose images by DL, and difference between dose and DL images.

	241.5 MeV/n	216 MeV/n	190 MeV/n
Measured SEB x-ray image	30 mm	35 mm	57 mm
Dose image	18 mm	28 mm	37 mm
Predicted dose images by DL	18 mm	24 mm	32 mm
Difference	0 mm	−4 mm	−5 mm

based on the measured data by the x-ray camera to accelerate the data generation process. Compare to conventional MC simulations, the model function could generate 10,000 SEB x-ray images for approximately 10 min on a regular personal computer.

In addition, the model function includes appropriate background low signal component so that the network trained with simulated data could be deployed to the measured data with high accuracy. In other words, the realistic SEB x-ray image with background low signal component has been correlated to the simulated dose image while training the proposed network. The background low signal component in the measured SEB x-ray images would not deteriorate the image quality of the DL-predicted dose images using our trained network. Our network trained with simulated data was thus

transferable on the measured data. The proposed network was also trained with simulated SEB x-ray images without background low signal component and deployed to the measured SEB x-ray images after post-processing by a variety of methods (data not shown). However, neither the dose images nor Bragg peak position and beam range could be predicted correctly due to the background low signal component inconsistency between the simulated and measured SEB x-ray images whether with post-processing or not.

The predicted dose images by DL could successfully convert the measured or simulated SEB x-ray images to the dose images. The predicted dose images by DL had clear Bragg peaks and the statistical noises were reduced or almost eliminated from the images. It suggests that noise resistance while converting different modality images is one of the advantages

TABLE VIII. MSE and SSIM for predicted dose images by DL from three measured SEB x-ray images.

Predicted dose images by DL	40 × 40	200 × 200	Ratio of 40 × 40/ 200 × 200
MSE: 241.5 MeV/n	0.25	1.6×10^{-3}	156
MSE: 216 MeV/n	0.30	5.5×10^{-3}	54
MSE: 190 MeV/n	0.12	7.3×10^{-4}	164
SSIM: 241.5 MeV/n	0.99	0.99	1
SSIM: 216 MeV/n	0.98	0.96	1.02
SSIM: 190 MeV/n	0.98	0.97	1.01
BP position error (mm): 241.5 MeV/n	0	0	–
BP position error (mm): 216 MeV/n	0	1.9	–
BP position error (mm): 190 MeV/n	0	0	–

MSE, mean squared error; SSIM, structural similarity index.

of deep learning-based approaches and similar results were reported in [28,29].

Despite the measured SEB x-ray images in size of 40 × 40, our model function could generate any larger matrix size of simulated dose images for spatial resolution enhancement. We took this advantage to design a deep learning network which can convert SEB x-ray images to dose images while upscaling the dimension of final dose images as the network outputs. The concept was demonstrated in this work with the matrix size of 200 x 200 for the final predicted dose images. The average MSE was improved by ∼ 100 folds for simulated testing data and by ∼ 125 folds for the three measured data as a result of the spatial resolution enhancement. The performance evaluation of the Bragg peak position error was not as intuitive as MSE or SSIM because the error was compared with the predicted dose images in their own matrix sizes. The 0 mm Bragg peak position error for the simulated testing data in size of 40 × 40 could only mean that the performance of the trained network was stable and reproducible. Although there was 1.9 mm Bragg peak position error for 216 MeV/n predicted dose images in size of 200 × 200, it was small enough compared to the errors estimated from the SEB x-ray images. Overall, the precision of the Bragg peak position and beam range estimation would be improved when the super resolution is also included in the proposed network. We have not found significant correlation between the prediction accuracy and the beam energies in this work, but a further investigation is needed.

The proposed network is comprised of two U-nets for image conversion and super resolution. These two U-nets can be trained together as Fig. 6 depicted, although we trained them using a two-step scheme because of the performance comparison for the two dimension configurations, that is, 40 × 40 and 200 × 200. Initializing the trainable parameters in the first U-net with the previous trained network was to accelerate the convergence process of the deep learning training. As mentioned, the same performance can be achieved if the two U-nets are trained together with the same training data with optimized hyperparameters.

In this pilot study, the major issue of limited amount of training data has been resolved by generating realistic simulated data using our in-house developed model function while the trained proposed DL network can be deployed on the noisy measured SEB x-ray images. To comprehensively evaluate the performance of the DL approach on SEB x-ray dose conversion for clinical carbon ion radiotherapy treatment planning, more measurements must be required under various conditions, such as wider range of beam setup and heterogeneous material, for future work. The network trained with the simulated data could be fine-tuned with newly acquired data for different measurement setup and accuracy improvement.

5. CONCLUSIONS

We have demonstrated the advantages of predicting dose images using our deep learning workflow not only for simulated data but also for measured data. For future work, we will investigate the deep learning-based approaches with more measured data acquired under different conditions.

CONFLICTS OF INTEREST

The authors have no conflicts to disclose.

ACKNOWLEDGMENTS

*These two authors are equally contributed to this manuscript
a)Author to whom correspondence should be addressed. Electronic mail: s-yama@met.nagoya-u.ac.jp; Telephone:+81-52-719-1559; Fax:+81-52-719-1559.

REFERENCES

1. Min CH, Kim CH, Youn M, Kim J. Prompt gamma measurements for locating dose falloff region in proton therapy. *Appl Phys Lett*. 2006;89:183517.

2. Kim CH, Park JH, Seo H, Lee HR. Gamma electron vertex imaging and application to beam range verification in proton therapy. *Med Phys*. 2012;39:1001–1005.

3. Kim D, Yim H, Kim J-W. Pinhole camera measurements of prompt gamma rays for detection of beam range in proton therapy. *J Korean Phys Soc*. 2009;55:1673–1676.

4. Kurosawa S, Kubo H, Ueno K, et al. Prompt gamma detection for range verification in proton therapy. *Curr Appl Phys*. 2012;12:364–368.

5. Smeets J, Roellinghoff F, Prieels D, et al. Prompt gamma imaging with a slit camera for real-time range control in proton therapy. *Phys Med Biol*. 2012;57:3371–3405.

6. Perali I, Celani A, Bombelli L, et al. Prompt gamma imaging of proton pencil beams at clinical dose rate. *Phys Med Biol*. 2014;59:5849–5871.

7. Richter C, Pausch G, Barczyk S, et al. First clinical application of a prompt gamma based in vivo proton range verification system. *Radiother Oncol*. 2016;118:232–237.

8. Polf J, Avery S, Mackin D, Beddar S. Imaging of prompt gamma rays emitted during delivery of clinical proton beams with a Compton camera: feasibility studies for range verification. *Phys Med Biol*. 2015;16:7085–7099.

9. Draeger E, Mackin D, Peterson S, et al. Polf, 3D prompt gamma imaging for proton beam range verification. *Phys Med Biol 63*. 2018;035019;13.

10. Bennett GW, Archambeau JO, Archambeau BE, Meltzer JI, Wingate CL. Visualization and transport of positron emission from proton activation in vivo. *Science*. 1978;200:1151–1153.

11. Guerra AD, Domenico DD, Gambaccini M, Marziani M. A Monte Carlo simulation of the possible use of positron emission tomography in proton radiotherapy. *Nucl Instr Meth A*. 1994;345:379–384.

12. Oelfke U, Lam GKY, Atkins MS. Proton dose monitoring with PET: quantitative studies in lucite. *Phys Med Biol*. 1996;41:177–196.

13. Hishikawa Y, Kagawa K, Murakami M, Sakai H, Akagi T, Abe M. Usefulness of positron-emission tomographic images after proton therapy. *Int J Radiat Oncol Biol Phys*. 2002;53:1388–1391.

14. Parodi K, Paganetti H, Shih EA, et al. Patient study on in-vivo verification of beam delivery and range using PET/CT imaging after proton therapy. *Int J Radiat Oncol Biol Phys*. 2007;68:920–934.

15. Litzenberg DW, Roberts DA, Lee MY, et al. On-line monitoring of radiotherapy beams: Experimental results with proton beams. *Med Phys*. 1999;26:992–1006.

16. Parodi K, Enghardt W, Haberer T. In-beam PET measurements of radioactivity induced by proton beams. *Phys Med Biol*. 2002;47:21–36.

17. Inaniwa T, Tomitani T, Kohno T, Kanai T. Quantitative comparison of suitability of various beams for range monitoring with induced activity in hadron therapy. *Phys Med Biol*. 2005;50:1131–1145.

18. Iseki Y, Mizuno H, Futami Y, et al. Positron camera for range verification of heavy-ion radiotherapy. *Nucl Instrum Methods-A*. 2003;515:840–849.

19. Nishio T, Ogino T, Nomura K, Uchida H. Dose-volume delivery guided proton therapy using beam on-line PET system. *Med Phys*. 2006;33:4190–4197.

20. Yamaya T, Yoshida E, Inaniwa T, et al. Development of a small prototype for a proof-of-concept of OpenPET imaging. *Phys Med Biol*. 2011;56:1123–1137.

21. Tashima H, Yamaya T, Yoshida E, Kinouchi S, Watanabe M, Tanaka E. A single-ring OpenPET enabling PET imaging during radiotherapy. *Phys Med Biol*. 2012;57:4705–4718.

22. Yamamoto S, Toshito T, Komori M, et al. Monitoring of positron using high-energy gamma camera for proton therapy. *Ann Nucl Med*. 2015;29:268–275.

23. Yamaguchi M, Torikai K, Kawachi N, et al. Beam range estimation by measuring bremsstrahlung. *Phys Med Biol*. 2012;57:2843–2856.

24. Yamaguchi M, Nagao Y, Ando K, et al. Secondary -electron-bremsstrahlung imaging for proton therapy, Nuclear Inst. and Methods in. *Phys Res-A*. 2016;833:199–207.

25. Ando K, Yamaguchi M, Yamamoto S, Toshito T, Kawachi N. Development of a low-energy x-ray camera for the imaging of secondary electron bremsstrahlung x-ray emitted during proton irradiation for range estimation. *Phys Med Biol*. 2017;62:5006–5020.

26. Yamaguchi M, Nagao Y, Ando K, et al. Imaging of monochromatic beams by measuring secondary electron bremsstrahlung for carbon-ion therapy using a pinhole x-ray camera. *Phys Med Biol*. 2018;63:045016.

27. Yamamoto S, Yamaguchi M, Akagi T, Sasano M, Kawachi N. Development of a YAP(Ce) camera for the imaging of secondary electron bremsstrahlung x-ray emitted during carbon-ion irradiation toward the use of clinical conditions. *Phys Med Biol 64*. 2019;64:135019.

28. Hwang D, Kim KY, Kang SK, et al. Improving the accuracy of simultaneously reconstructed activity and attenuation maps using deep learning. *J Nucl Med*. 2018;59:1624–1629.

29. Hwang D, Kang SK, Kim KY, et al. Generation of PET attenuation map for whole-body time-of-flight 18F-FDG PET/MRI using a deep neural network trained with simultaneously reconstructed activity and attenuation maps. *J Nucl Med*. 2019;60:1183–1189.

30. Liu C, Li Z, Hu W, Xing L, Peng H. Range and dose verification in proton therapy using proton-induced positron emitters and recurrent neural networks (RNNs). *Phys Med Biol*. 2019;64:175009.

31. Masuda T, Nishio T, Kataoka J, Arimoto M, Sano A, Karasawa K. ML-EM algorithm for dose estimation using PET in proton therapy. *Phys Med Biol*. 2019;64:175011.

32. Ronneberger O, Fischer P, Brox T. U-net: convolutional networks for biomedical image segmentation. *Medical Image Computing and Computer-Assisted Intervention (MICCAI)*. New York, NY: Springer; 2015:234–241.

33. Kamada T, Tsujii H, Blakely EA, et al. Carbon ion radiotherapy in Japan: an assessment of 20 years of clinical experience. *Lancet Oncol*. 2015;16:e93–e100.

34. Sato T, Niita K, Matsuda N, et al. Particle and heavy ion transport code system PHITS, Version 2.52. *J Nucl Sci Technol*. 2013;50:913–923.

35. Renieblas GP, Nogués AT, González AM, Gómez-Leon N, Del Castillo EG. Structural similarity index family for image quality assessment in radiological images. Journal of Medical. *Imaging*. 2017;4:035501.

SUPPORTING INFORMATION

Additional supporting information may be found online in the Supporting Information section at the end of the article.

Supplemental Material. Measured and predicted six images with 10 s irradiations for 17 cm diameter cylindrical water phantom during irradiation of 241.5 MeV/n carbon ions.